X-ray Periodicities in Sources Observed by the RXTE ASM

by

Vasudha B. Shivamoggi

Submitted to the Department of Physics
in partial fulfillment of the requirements for the degree of

Bachelor of Science in Physics

at the

MASSACHUSETTS INSTITUTE OF TECHNOLOGY

May 2005 [June 2005]

Author . . . .
Department of Physics
May 13, 2005

Certified by . . . .
Alan M. Levine
Center for Space Research
Thesis Supervisor

Accepted by . . . .
David E. Pritchard
Senior Thesis Coordinator, Department of Physics

X-ray Periodicities in Sources Observed by the RXTE ASM

by

Vasudha B. Shivamoggi

Submitted to the Department of Physics
on May 13, 2005, in partial fulfillment of the
requirements for the degree of
Bachelor of Science in Physics

Abstract

The X-ray intensities measured from 230 X-ray sources observed by the *RXTE* All-Sky Monitor (ASM) were analyzed for periodic behavior. The ASM has been observing sources for nine years in the 1.5-12 keV energy range. In this search, we investigated a frequency range of 5 d^{-1} to 144 d^{-1} for periodic modulation. The search was carried out by applying the Fast Fourier Transform on the ASM data and whitening the resulting power density spectrum using a local averaging technique. A power threshold was set to determine the statistical significance of a peak in the power density spectrum. The search verified the orbital frequencies of four known X-ray binaries and also identified four previously unreported periodicities. The 5.7232 d^{-1} orbital frequency of GX 9+9 was observed for the first time in ASM data, although this modulation had been observed before. The 6.0999 d^{-1} peak found for XTE J1723-376 has not been reported before and may be an orbital frequency.

Thesis Supervisor: Alan M. Levine
Title: Center for Space Research

Acknowledgments

I would like to thank Dr. Alan Levine and Prof. Saul Rappaport for many helpful discussions and suggestions. Their expertise and advice have made this thesis possible. I owe much gratitude to Abigail Bushman, whose encouragement was unfailing every step of the way. Many thanks to my sister Rohini, the original astrophysicist, for her persistent enthusiasm for my work. Last, but certainly not least, I am grateful to my parents Bhimsen and Jayashree, who inspired me to dream of great things and gave me the love and support to reach for them.

Contents

List of Figures

List of Tables

Chapter 1

Introduction

X-rays are very high-energy photons with energies between about 1 keV and 100 keV. They are emitted when energetic electrons undergo collisions with atoms. The rapid deceleration of the electron can sometimes cause an electron from the inner shell to be ejected out of its atom. As electrons from higher energy levels transition to the empty shell, they emit X-ray photons. In this study, we examine X-rays emitted by neutron stars and black holes, which are the final stages in the lifetime of massive stars. These objects can exist in a binary system with a companion star. In the case of an X-ray binary, matter from the companion star accretes onto the neutron star or black hole, and eventually becomes hot enough to emit X-rays. The X-ray signal from the source is modulated at frequencies corresponding to the neutron star spin frequency and the orbital frequency of the binary system. We analyze data from the *RXTE* ASM to search for periodicities in the 5 d^{-1} to 144 d^{-1} range. In this chapter, I will present theoretical topics related to stellar evolution and X-ray binaries. Chapter 2 describes the instrumentation of the ASM. Chapter 3 contains an outline of data analysis techniques. Chapter 4 describes search methods and gives the results of the search.

1.1 Star Deaths

A review of the processes of stellar evolution can be found in [1]. I will briefly discuss these processes in this section. Stars spend the vast majority of their lives releasing energy by burning hydrogen in their cores. The gas that comprises a star is held together by gravitational forces, but kept from further collapse by internal pressures. The resulting hydrostatic equilibrium keeps the star at approximately the same size throughout its hydrogen-burning lifetime.

When the hydrogen in the core has been completely turned into helium, however, fusion processes stop. Without pressure to counteract gravitational collapse, the core contracts quickly, drawing in matter from a shell immediately around the core. Eventually, this process heats up the shell sufficiently to allow hydrogen burning in the region. When the hydrogen in the shell is also exhausted, the core again contracts and heats up rapidly. Energy propagates outward through the star, causing the stellar envelope to expand. As the star's surface area increases, its surface temperature drops, and it becomes a red giant.

Meanwhile, the core is still contracting and becoming hotter. If the star's mass is high enough, temperatures will increase enough to ignite the fusion of helium into carbon and even ignite the burning of carbon. The contraction of the core releases vast amounts of thermal energy, which cause the star to pulsate and eject the outermost layers of gas. Known for historical reasons as a planetary nebula, the gas expands away from the star, leaving a very small, very dense core.

The fate of the stellar core is now determined by its mass. If the mass is below 1.4 solar masses (the Chandrasekhar limit), gravitational forces cause it to contract until it reaches a density on the order of 10^9 kg/m^3 [2]. For comparison, the average density of the Earth is about 5.4×10^3 kg/m^3. Called a white dwarf, the star is kept from further collapse by the repulsive pressure of the degenerate 0 gas. The electrons in the star are so closely packed that the Pauli Exclusion principle prevents them from collapsing further. Gravitational forces are now balanced, not by fusion, but by repulsive degenerate Fermi pressure. This equilibrium proves to be very stable, and the star remains as a white dwarf.

If the stellar core is more massive than the Chandrasekhar limit, even the degenerate electron pressure cannot balance the strong gravitational tendency to collapse. As the core contracts further, the protons and electrons are crushed together to form neutrons. Beyond a density of 10^{17} kg/m^3, the quantum exclusion principle for neutrons becomes a significant factor. The pressure due to the degenerate neutron gas balances the gravitational contraction if the star's mass is less than about 3 solar masses (the exact value of this limit is still not well determined), and the star becomes a neutron star. Densities in neutron stars reach fantastically high values. For example, a solar mass neutron star would have a radius of about ten kilometers. If the stellar mass is greater than 3 solar masses, nothing can stop collapse to a black hole. As the core collapses, the outer layers of the star rebound violently and are ejected from the neutron star. These supernova explosions can release up to 10^{44}J, which is roughly equal to the energy output of the sun during its lifetime of 10^{10} years.

If a neutron star is rotating and has a strong magnetic field, it may be a pulsar. Pulsars are strongly magnetized, rotating neutron stars that emit a periodic electromagnetic signal. Some of the strongest magnetic fields ever measured have been observed on pulsars. Typical pulsars have a dipolar magnetic field with a strength on the order of 10^8 T at the surface.

1.2 X-ray Binary Systems

In our search, we investigate neutron stars or black holes (called compact objects) that exist in a binary system with a companion star. Refs. [3] and [4] provide a detailed review of the properties and observations of X-ray binaries, but I will briefly summarize relevant points here. An X-ray binary occurs when a compact object accretes matter from a companion star, either due to transfer of matter through the inner Lagrangian point or from the stellar wind of the companion (see Figure 1-1). There are approximately a few hundred X-ray binaries in our galaxy [4]. This extremely small fraction of the total number of stars in the galaxy reflects how many

Figure 1-1: A compact object accreting matter from its companion [5].

rare events must occur in order for an X-ray binary to form.

There are many obstacles to the formation of an X-ray binary system. For example, the precursors of compact objects (red giants and the like) are too large to fit into the small binary orbits we observe. Even more troubling, the supernova explosion that creates the compact object should blow the companion away. A possible resolution to this problem is a model of asymmetric supernova explosions that could leave the companion intact [6]. Another possibility is that the compact object binds a companion *after* the explosion.

X-ray binaries can be divided into two categories, depending on the mass of the compact object's companion. In a Low Mass X-ray Binary (LMXB), the companion's mass is less than that of the compact object. An accreting LMXB is characterized by a companion star that fills its Roche Lobe. The Roche Lobe is defined as the region inside the marginal equipotential surface between the two sources. The potential is calculated in a reference frame that rotates with the orbital period of the binary system. In Figure 1-2, the dashed lines mark the effective equipotential where matter is marginally bound to the system. The apex, where this potential intersects itself, is called the inner Lagrangian point. When the companion fills its Roche Lobe, matter can overflow through the inner Lagrangian point and become bound to the compact object. This mechanism of mass transfer proves to be a very stable one as long as the mass of the companion remains less than the mass of the compact object. The

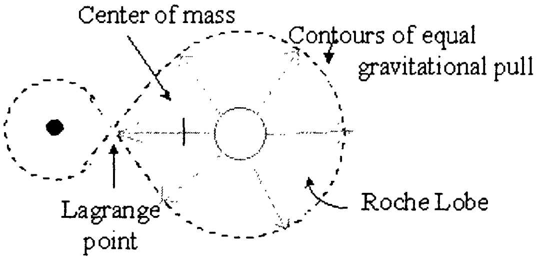

Figure 1-2: Roche Lobe configuration of a binary system The dashed lines mark surfaces of constant effective potential, rather than force [7].

lifetime of the LMXB typically ranges from 10^7 to 10^9 years. Because the stars in a LMXB are so old, these systems are usually found in the galactic center or in globular clusters.

Some exotic types of LMXB's include the Accretion Disk Corona (ADC) sources and dippers. The ADC sources are characterized by a hot corona that completely surrounds the compact object. X-rays emitted close to the compact object's surface are scattered by electrons in the corona, resulting in less clearly-defined X-ray eclipses. In dipper sources, X-ray eclipses aren't caused by the companion at all, but by the splash of matter onto the accretion disk. The splash can well up into the line of sight, obscuring our view of the compact object and thus causing an eclipse.

An X-ray binary in which the mass of the companion exceeds a few solar masses is called a High Mass X-ray Binary (HMXB). The companion can be a hot O or B type star that doesn't fill its Roche Lobe. Instead, mass loss is driven by a strong stellar wind. A typical O type star will lose on the order of a few solar masses during its main sequence lifetime. Material blown away by the stellar wind can be captured gravitationally by the compact object and drawn into an accretion disk. The lifetime of a HMXB is determined by the evolution of the companion star, and follows the typical lifetime of an O or B type star. For a companion losing matter through a stellar wind, this lifetime is usually about 10^6 years [1]. Most HMXB's are found along with other young stars in the galactic plane. The magnetic fields of compact objects in HMXB's are usually much stronger than their LMXB counterparts. This is because in these relatively short-lived systems, the magnetic field hasn't had time to evolve away. If an accreting compact object has a strong magnetic field, this field can drive accretion-powered pulsars (see below).

Optical observations can be very useful in classifying a compact object as a LM- or HMXB. By observing the spectral type of the companion (O or B for a HMXB; later types for a LMXB), it is possible to determine the mass of the companion star. Optical observations are difficult to make for a LMXB because the accretion disk of the compact object is usually very luminous and outshines the companion. In some instances, however, accretion disk luminosities can diminish, revealing a faint optical companion.

After the matter has transferred to the disk of the neutron star – either through the inner Lagrangian point or due to the companion's stellar wind – it loses angular momentum to the star at a high rate. Angular momentum transport in the disk can be achieved through thermal processes or through magnetohydrodynamic (MHD) instabilities. Interaction with the neutron star's magnetic field can cause macroscopic instabilities. These can in turn lead to fully developed MHD turbulence, which is an efficient mechanism of angular momentum transport.

The geometry of the accretion disk depends on angular momentum losses and also on the efficiency of radiative losses. If accreting matter can radiate effectively, it will be cool and form a thin accretion disk. If radiative processes are not efficient, the accretion flows are hot, and the disk will be thick.

1.3 Pulsars

Neutron stars exchange angular momentum with the matter accreting around them through their very strong magnetic fields. These fields rotate with the same period as the star, and provide a coupling mechanism between the star's surface and the accreting matter [4]. The relevant length scale to consider is the Alfven radius, defined as the radius where dynamics due to the stellar magnetic fields become comparable to thermal effects. Matter in the accretion disk rotates at the Kelperian frequency

Ω, where $\Omega^2 = \frac{GM}{R^3}$. Whether or not the matter can accrete onto the neutron star depends on its orbital frequency ν_{accret} relative to the spin frequency of the neutron star, ν_{ns}. If $\nu_{accret} < \nu_{ns}$, the matter cannot co-rotate with the star. The gas does not have sufficient angular momentum to overcome the centrifugal barrier of the neutron star. Instead of accreting onto the star, the gas is flung outwards. On the other hand, if $\nu_{accret} > \nu_{ns}$, coupling to the magnetic fields forces the accreting matter into co-rotation with the star. This material is now orbiting less rapidly than before; the missing angular momentum has been fed to the neutron star and contributes to an increase in its spin frequency.

If material attached to a magnetic field line accretes onto the neutron star, the resulting transfer of angular momentum to the star can drive a pulsar. Magnetic field lines channel the accreting matter onto the magnetic polar caps of the neutron star. As the gas falls towards the stellar surface, its gravitational potential energy is converted into kinetic energy. The gas heats up rapidly, eventually becoming hot enough to emit X-rays. If the magnetic poles are off-set from the rotational poles of the neutron star, a distant observer will see strong emission every time the magnetic pole rotates into view. In this way, pulsars emit a highly periodic X-ray signal at the spin frequency of the neutron star.

As noted above, spin-up is the increase of a neutron star's spin frequency due to angular momentum transfer from accreting matter. However, if the magnetic field lines of the neutron star extend above the inner region of the accretion disk, they will trap matter that is rotating with a relatively low orbital frequency. In this case, interaction with the magnetic field transfers angular momentum from the star to the rotating matter, resulting in spin-down. Both spin-up and spin-down processes occur at a given star, balancing out into a fairly stable spin frequency.

1.3.1 Slow Accretion Powered Pulsars

Calculations of the torques exerted by accreting matter and stellar magnetic fields show that a neutron star with a dipolar magnetic field of 10^{10} gauss at the surface will rotate in equilibrium at about 0.1 Hz. This class of pulsars is known as the slow accretion powered pulsars. They occur mostly in HMXB's, where the magnetic fields are still strong enough to impact accretion flows.

1.3.2 Millisecond Accretion Powered Pulsars

Pulsars that emit X-ray radiation at frequencies on the order of 200-600 Hz are called millisecond accretion powered pulsars. Millisecond pulsars are thought to be a later stage of a neutron star in a LMXB. Over the long lifetime of the companion star, the neutron star gradually loses its magnetic field and spins down. If the companion evolves, however, and overflows its Roche Lobe, accreting matter can reactivate the pulsar. Most of the observed millisecond pulsars have very evolved low-mass companions such as a white dwarf.

Chapter 2

Instrumentation

The Rossi X-ray Timing Explorer (RXTE) is an Earth-orbiting spacecraft that investigates X-ray sources. The spacecraft has been taking data since February 1996 as it orbits the Earth every 96 minutes. The All-Sky Monitor (ASM) on the RXTE is designed to provide nearly real-time information about the transient and outburst behavior of X-ray sources. The ASM is made up of three scanning shadow cameras (SSCs) that are mounted on a motorized drive [8]. Each SSC is a "Dicke" camera [9] that is made up of a position-sensitive proportional counter (PSPC) behind a slit mask. The mask provides the position resolution of the instrument: when X-rays from a distant source impinge on the ASM, the mask creates a shadow on the PSPC. The mask itself consists of 12 subsections, each containing about 15 open slits and 16 closed slits arranged in a pseudorandom pattern. X-ray photons impinging on the ASM from distant sources will cast shadows on the cameras that depend on the slit arrangement. The resulting shadow pattern is used to determine where in the field of view the photons came from. Each SSC has a field of view of $6^0 \times 90^0$ at FWHM.

The PSPC inside each SSC is a sealed proportional counter filled with a mixture of xenon and CO_2 gas kept at 1.2 atm. Inside the chamber, eight electrically-resistive anodes provide the main detecting mechanism. When an X-ray enters the chamber, it causes the ejection of electrons through the photoelectric effect. This process creates a population of electrons and ions in the chamber whose size is proportional to the energy of the X-ray photon. The electrons are attracted to anodes that are held at a positive potential relative to the chamber. Preamplifiers then measure the amount of charge received at the ends of the anodes. The ratio of pulse intensities at either end of an anode depends on where along the anode the avalanche originally occurred. Thus by recording the ratio of the pulse sizes, we can determine the position of an X-ray event. The energy of the X-ray photon can be determined by the sum of the pulse heights. The gain of the PSPC detectors was initially calibrated using the 6 keV X-rays emitted from a weak ^{55}Fe source aboard the spacecraft. The PSPC detectors and electronics are sensitive to X-rays with energy between 1.5 and 12 keV. Once the data has been sent back to the Earth, additional processing separates detections into three energy bands: 1.5-3 keV, 3-5 keV, and 5-12 keV [8].

The combination of the slit mask and PSPC detectors achieves a position resolution of 3' × 15' for strong sources. For weak sources, the resolution is $0.2^0 \times 1^0$ [9]. The ASM is sensitive to about 30 mCrab for a source at the center of the field of view [9]. The SSCs focus on one field of view for 90 s at a time, resulting in data sets or "dwells" of 90 s each. The motorized rotation drive rotates the SSCs in steps of 6^0, allowing the configuration to make a full rotation in about 100 minutes. The ASM is shut off for part of each orbit, however, to avoid high-flux observations that would damage the instrumentation. In practice, the ASM is able to scan about 40% of the sky during each 96 minute orbit of the satellite.

Chapter 3

Data Analysis Methods

3.1 Preliminary Analysis

Periodicities in the intensities of sources observed by the ASM can be identified with the help of Fast Fourier Transforms (FFT) of the ASM light curves. The ASM data are first corrected for the Earth's orbital motion around the sun in a process called barycenter-correcting. The Earth orbits the sun in a closed trajectory. If we consider its motion relative to a distant source, it spends part of the year moving away from it and part of the year approaching it. While the Earth is approaching the distant source, an observer on the Earth will find that a periodic signal from the source appears blue-shifted. On the other hand, the data train will appear red-shifted while the Earth is moving away from the source. This modulation of the signal is the result of the Earth's motion, not an intrinsic pulsation of the source. The process of barycenter-correcting modifies the data so that the data look like the satellite was at the barycenter, or center of mass, of the solar system rather than in orbit around the sun. The ASM observes sources in 90-second dwells. For easier manipulation of the data set, we rebin the data into larger time bins. The barycenter-corrected data were rebinned in 5-minute time bins, which corresponds to a Nyquist frequency of $\frac{1}{10}$ min^{-1}. The Nyquist frequency is the highest frequency discrete in a Fourier transform; therefore 0.1 min^{-1} or 144 day^{-1} represents the upper bound on the frequencies investigated by this search. In a typical Fourier transform,

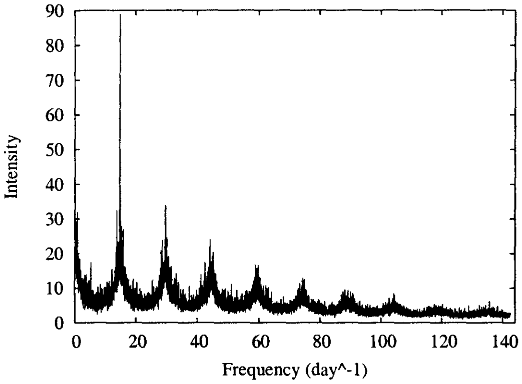

Figure 3-1: Power density spectrum of Sco X-1 after maximum rebinning

the frequencies are integer multiples of $\frac{1}{T}$, where T is the time interval of the data train. These frequencies then have a resolution of $\frac{1}{T}$. To obtain better precision in frequency, we oversample the data by a factor of 4, improving the frequency resolution to $\frac{1}{4T}$. The oversampling is achieved by adding three times the number of original bins to the end of the data train, and filling the additional bins with 0's. The FFT is then applied to the barycenter-corrected and rebinned ASM data. Finally, the power density spectrum of the FFT is computed and normalized so that the average of the spectrum is 1. A periodicity will appear in the power density spectrum of the FFT as a sharp peak at a certain frequency.

The resulting power density spectrum consists of nearly 2 million frequency bins. Because this is an unwieldy number of data points to plot, the spectrum is reduced using a rebinning technique described below. The power density spectrum is divided into blocks of 300 frequency bins. For each block, we find the frequency with the highest power and discard the other data points. This method reduces the number of data points by a factor of 300 while retaining the frequencies with the highest power, i.e., the periodicities we are seeking.

Figure 3-1 shows a power density spectrum of Scorpius X-1 (Sco X-1) obtained through the above steps. The most prominent feature in the spectrum is the presence of a strong, broad peak at 15 day^{-1} and its harmonics. The *RXTE* satellite orbits the Earth every 96 minutes, corresponding to a frequency of 15 d^{-1}. We note empirically that this peak is an artifact of the orbital motion of the satellite around the Earth, although the exact mechanism for the peak's appearance is unclear. The harmonics of the 15 d^{-1} peak are also readily apparent, and can be seen at 30 d^{-1}, 45 d^{-1}, 60 d^{-1}, and so on.

A peak at 1 d^{-1} appears on the power density spectrum, corresponding to the 1 d^{-1} rotation cycle of the Earth. In addition, we also observe beats of the 1 d^{-1} peak with the 15 d^{-1} peak and its harmonics. To calculate the frequencies of beats between two peaks, we consider a source whose signal is modulated by two different sinusoidal signals. The data will appear as a constant multiplied by the sinusoidal signals:

$$d = d(t_{j_0})\ \cos(\omega_1 t_j + \phi_1)\ \cos(\omega_2 t_j + \phi_2) \tag{3.1}$$

Using trig identities, Eq. (3-1) can be rewritten as

$$d = d(t_{j_0})\ \{\cos[(\omega_1 + \omega_2)t_j + \phi\prime_1] - \cos[(\omega_1 - \omega_2)t_j + \phi\prime_2]\} \tag{3.2}$$

From Eq. (3-2), we can see that the Fourier transform will result in peaks at $\omega_1+\omega_2$ and $|\omega_1$ - $\omega_2|$. Applying this result to the ASM data, we expect to see harmonics at 14 d^{-1}, 16 d^{-1}, 29 d^{-1}, 31 d^{-1}, and so on. These features were observed in many strong sources.

Peaks at these frequencies are common to all the sources observed by the ASM, and we discard these peaks as artifacts. The presence of a strong peak at a frequency not listed above would suggest a periodic modulation in the source itself.

3.2 Whitening Methods

The artifacts at 15 d^{-1} and its harmonics introduce a high level of noise into the power density spectrum. This can obscure the presence of a true periodic modulation by making it more difficult to detect. Thus the first step in searching for periodicities is to find a way to remove or weaken the artifacts discussed in Section 3.1. One method that immediately comes to mind is to calculate an ensemble average of spectra of all the sources observed by the ASM. Dividing each spectrum by the ensemble average would then reduce the powers at the frequencies of artifacts present in the power density spectra of many sources. In practice, however, this method is not useful. The ASM data are not uniform in intensity, and a meaningful ensemble average is not straightforward to compute. The strength of the 15 d^{-1} peak, for example, is different in each source. Dividing the power density spectrum of a strong source by an ensemble average would not remove this artifact.

Instead we divide each power density spectrum by a local average computed from that spectrum itself. Dividing each point by a local level of noise has the effect of reducing broad peaks. This helps to weaken the presence of the 15 d^{-1} signal and its harmonics, which tend to be broad peaks. On the other hand, real periodic modulations will be very sharp. To avoid reducing these peaks in our averaging method, we compute the local average around a given frequency *without* including the power at the frequency itself. Thus the very narrow peaks that we are looking for will not be reduced as much as wide peaks. In addition to reducing the strength of artifacts, the local averaging process has the effect of whitening the power density spectrum. The distribution of the intensity points becomes more Gaussian after local averaging.

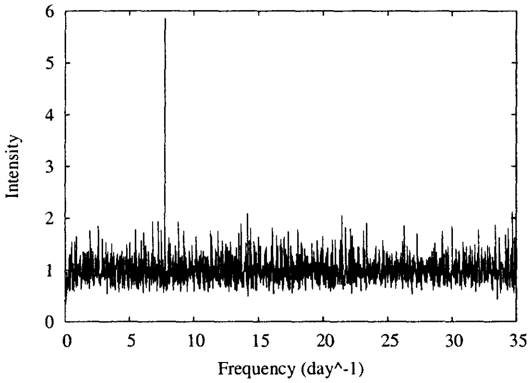

Figure 3-2: Power density spectrum of AM Her after maximum-rebinning and local averaging

Three different methods of implementing the whitening technique were tried. The criterion for selection of the best method was the signal-to-noise ratio for a known periodicity. The first method tested involved first using the rebinning technique described in Section 3.1 to select the strongest amplitudes out of every 300 frequency bins. The rebinned spectrum was then whitened using the local averaging technique. Figure 3-2 shows the resulting power density spectrum for AM Herculis (AM Her), a cataclysmic variable source with a known orbital frequency of 7.7564 ± 0.0007 d^{-1} [10]. When carrying out the local averaging, we tried various widths and settled on the width that resulted in the weakest artifacts. For the spectrum shown in Figure 3-2, this width was 10 rebinned frequency bins, corresponding to 3000 original frequencies. Thus each point was divided by the average of intensities of the 10 bins to its left and the 10 bins to its right. At the edges, where ten bins were not available on one side, the averaging technique was modified to include all the remaining bins until the edge, and an equal number of bins on the other side of the point. For example, the local average at bin 4 was computed by adding the intensities of bins 1-3 and 5-7, and dividing by 6. It is important to note that the power density spectrum has been rebinned, and thus each frequency bin represents 300 original frequency bins. Figure 3-2 shows that the artifacts at 15 d^{-1} and 30 d^{-1} have disappeared, leaving a clear periodic signal at 7.75644 d^{-1}. This value agrees with the frequency in [10].

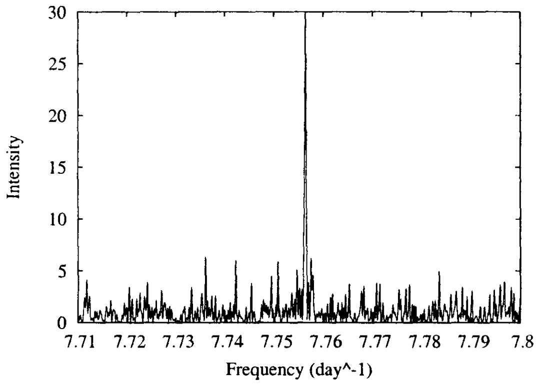

Figure 3-3: Power density spectrum of AM Her before maximum-rebinning or local averaging

Figure 3-3 shows a frequency range around the peak in the original power density spectrum before it has been maximum-rebinned or divided by the local average. To calculate the uncertainty in the frequency of a given peak, we divide the FWHM from Figure 3-3 by the statistical significance of the peak in terms of the equivalent standard deviations σ. To find σ, we note that the powers in the power density spectra are exponentially distributed, and the probability of a statistical fluctuation given a peak with power $\geq$ x is therefore given by

$$e^{-x} = \int_{\sigma}^{\infty} \frac{1}{\sqrt{2\pi}} e^{-\frac{t^2}{2}} dt \tag{3.3}$$

We can simplify Eq. (3-3) in terms of the error function,

$$e^{-x} = \frac{1}{2} \left[1 - \mathrm{erf}(\sigma)\right] \tag{3.4}$$

The peak shown in Figure 3-3 has a FWHM of three frequency bins and an amplitude of 29.945, corresponding to an uncertainty of 0.00009 d^{-1}.

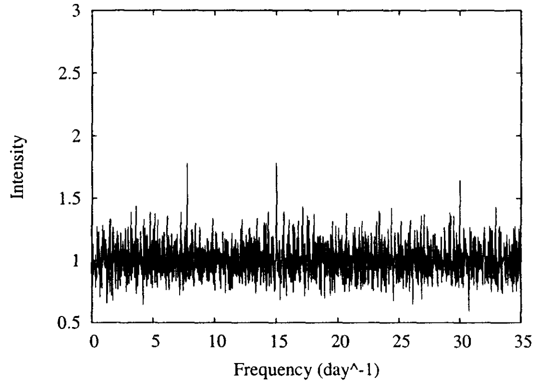

Figure 3-4: Power density spectrum of AM Her after average-rebinning and local averaging

Figure 3-4 shows a locally averaged spectrum of AM Her obtained in a slightly different way. The original power density spectrum was rebinned by computing the average intensity of each block, rather than the maximum. The median frequency of the block, together with its mean intensity, are retained as the rebinned spectrum. Comparing Figures 3-2 and 3-4, we see that this method is not as effective in reducing the presence of artifacts. The orbital frequency at 15 d^{-1} and its first harmonic at 30 d^{-1} are almost as strong as the real periodicity.

Finally, we tried using the average-rebinned spectrum as a whitening method. For

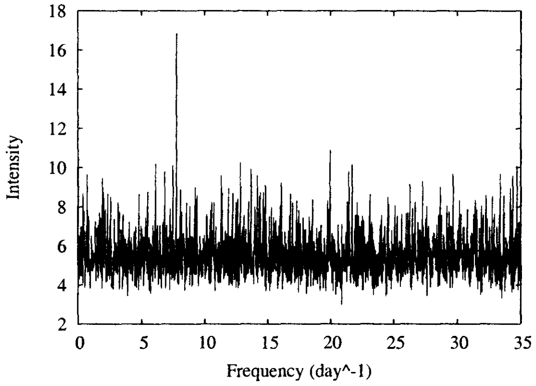

Figure 3-5: Power density spectrum of AM Her computed by dividing the maximum-rebinned spectrum by the average-rebinned spectrum.

a given source, the power density spectrum was reduced by computing the average amplitude of each block of 300. Next, the power density was calculated by taking the maximum amplitude of each block. Figure 3-5 shows the spectrum resulting from dividing each amplitude in the maximum-rebinned spectrum by the corresponding amplitude in the average-rebinned one. Although the periodicity at 7.76 d^{-1} is the strongest peak in the spectrum, it is not as strong relative to the baseline as the peak seen in Figure 3-2.

After comparing the three methods for AM Her and other sources with known periodicities, we chose the first for our whitening technique. Following preliminary analysis as described in Section 3.1, the power density spectra were rebinned using the maximum of 300 frequency bins and then divided by the local average. Figures 3-6 through 3-8 illustrate the whitening process for Sco X-1. Figure 3-6 shows the power density spectrum after the original spectrum has been maximum-rebinned. The local average of the spectrum, computed without including the point itself, is shown in Figure 3-7. As expected, the local average exhibits the broad peaks of the 15 d^{-1} orbital frequency and its harmonics. Figure 3-8 shows the result of dividing the rebinned spectrum by its local average. The wide peaks from the un-whitened spectrum are no longer present, with the exception of a narrow signal at 15 d^{-1}. Because this signal is confined to a single frequency bin, we can easily ignore it in our search for real periodicities.

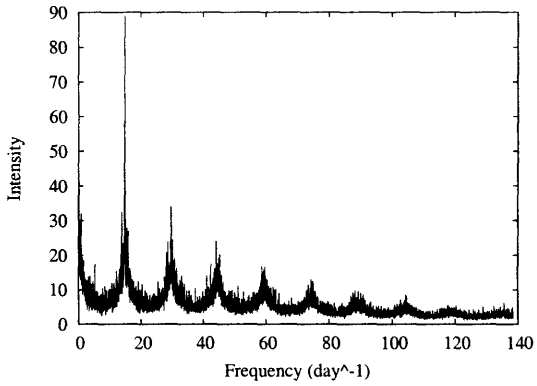

Figure 3-6: Power density spectrum of Sco X-1 after maximum-rebinning.

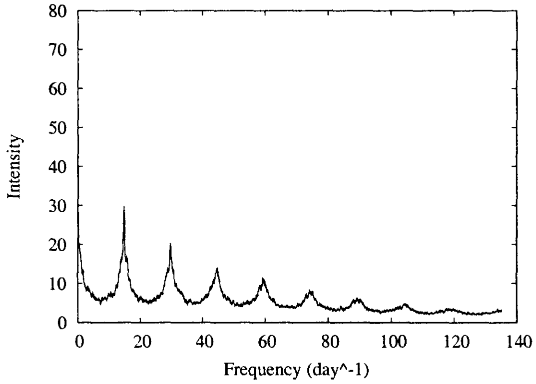

Figure 3-7: Local Average of Sco X-1

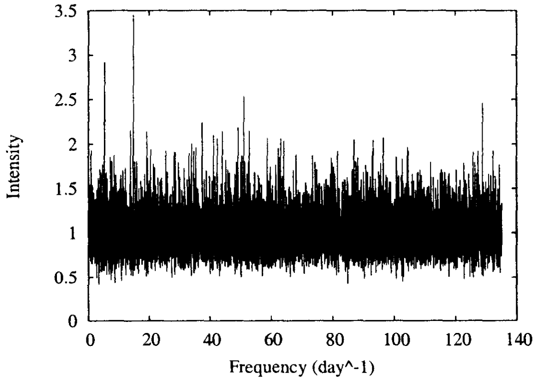

Figure 3-8: Power density spectrum of Sco X-1 after maximum-rebinning and local averaging

3.2.1 Statistics

The whitening technique described above removes red-noise from the power density spectrum, resulting in more or less Gaussian noise. The power intensities of an FFT with Gaussian noise are characterized by an exponential distribution. The probability that a given power intensity is greater than some threshold x_0 is given by

$$\text{prob}(x > x_0) = e^{-x_0/x_{av}} \tag{3.5}$$

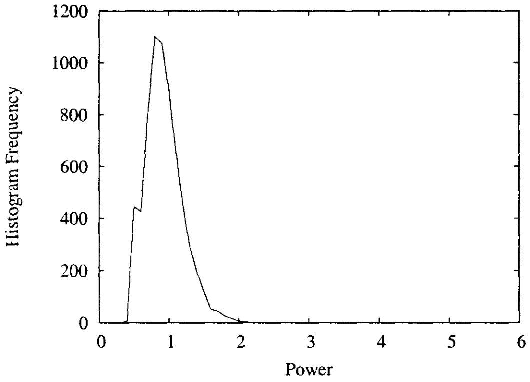

Figure 3-9: Power density spectrum of Sco X-1 after rebinning and local averaging

As noted above, the power density spectrum was normalized so that the average was 1. Thus $x_{av} = 1$ in Eq.(3-5). Figure 3-9 shows a histogram of the powers in the power density spectrum of AM Her shown in Figure 3-2. Because the power density spectrum (as seen in Figure 3-2) has a mean baseline of about 0.9, the histogram shows a maximum at an intensity of 0.9 instead of 0. As expected from Eq. (3-5), however, the histogram has an exponential tail for intensities higher than the baseline.

Chapter 4

Search Methods and Results

4.1 Setting a Threshold

After the sources have been analyzed using techniques described in Chapter 3, the power density spectra must be examined for strong peaks. Because we analyzed 230 sources in 4 energy bands, it was impractical to examine each power density spectrum by hand. To automate the process of determining whether a strong peak in the power density spectrum was statistically significant, we set a threshold for power amplitude. A power in the spectrum stronger than this threshold and not located in a frequency range known to be an artifact, is a candidate for a true periodicity. An initial value for the threshold is computed by fixing beforehand the number of statistical fluctuations we expect to find. This is to ensure that we do not find too many peaks in the search that are simply due to statistics. For the purposes of this search, we set the number of expected statistical fluctuations peaks to be 1. The power threshold is then calculated as the value of x_0 in Eq.(3-3) that would result in 1 peak observed across all frequency bins of all sources and energy bands analyzed.

To find this value of x_0, we first determine the total number of frequency bins investigated by this search. This total is given by

$$N = FRN_sE \tag{4.1}$$

where F is the number of frequency bins in a maximum-rebinned power density spectrum, R is the number of frequency bins in each rebinning block, N_s is the number of sources analyzed, and E is the number of energy bands investigated. In our search, we study the 230 brightest sources observed by the ASM, which records data in 4 energy bands. R is 300, and F is 6635. Substituting these values into Eq. (4-1), the total number of frequency bins becomes 1.83×10^9 bins. Thus we are seeking a value of x_0 that makes the probability of an intensity greater than x_0 equal to $1/1.83\times10^9$. Using Eq. (3-5), and noting that $x_{av} = 1$, we find that $x_0 = 21.33$.

The above process applies to a power density spectrum after FFT, while the spectra we are examining have been rebinned in blocks of 300 frequency bins and divided by the local average. To calculate the real intensity threshold, we must therefore divide our initial threshold x_0 by a value for the local average.

We estimate the intensity of the local average as the median value of the block-maximum when the original power density spectrum is rebinned. Denoting the median block maximum x_{max}, we make the following definition

$$P_m = \text{prob}(x < x_{max}) \tag{4.2}$$

For a given value of x_{max}, P_m is the probability that a power x is weaker than x_{max}. P_m^{300} is then the probability that x_{max} is greater than all the powers in a block of 300. But x_{max} is defined as the median maximal value; therefore it is the block maximum half of the time. P_m thus satisfies

$$P_m^{300} = \frac{1}{2} \tag{4.3}$$

Eq. (4-3) allows us to compute the value of P_m to be 0.99769.

Given P_m, the probability that an intensity point is greater than x_{max} is given by

$$\text{prob}(x > x_{max}) = 1 - P_m = e^{-x_{max}} \tag{4.4}$$

where the right-hand side follows from the assumption that the intensities are exponentially distributed. We can solve Eq. (4-4) for x_{max}, finding that $x_{max} = 6.07$. This value represents the median of a distribution of the maximum values of a maximum-rebinned spectrum. The calculation was tested empirically by generating a set of exponentially distributed data points (as we assume the power density spectrum of an FFT to be). This data set was then rebinned by taking the maximum of blocks containing 300 points each. Finally, the median of this set was calculated, and found to be between 6.04 and 6.08, indicating good agreement with the above calculation.

Now we are ready to set an intensity threshold. Dividing x_0 by x_{max} gives an intensity $I_0 = 3.51$. In the search for periodicities, a peak stronger than this threshold was considered statistically significant. By construction, we expect to find on the order of 1 power stronger than I_0 due to statistical fluctuations.

4.2 General Notes on Search Methods

After the threshold was set, we were ready to search the power density spectra that had been maximum-rebinned and whitened for peaks that exceeded I_0. We rejected peaks that appeared in the frequency ranges corresponding to known artifacts. These include the 1 d^{-1} orbital frequency of the Earth, and the 15 d^{-1} orbital frequency of the satellite. Most sources also exhibited harmonics of the satellite frequency, and we rejected peaks at these frequencies as well. The signals that appeared in most power density spectra were broader than one maximum-rebinned frequency bin, and we excluded regions of 0.1 d^{-1} around the frequencies described above. The power density spectra of many bright sources also displayed beats between the 1 d^{-1} frequency and the 15 d^{-1} frequency and its harmonics. To reject these artifacts, we also excluded the frequencies around the beats. Lastly, it was observed empirically that a high level of red noise exists at very low frequencies of the power density spectra. In particular, the DC component was the strongest peak in most spectra examined. Since the main purpose of this search was to identify periodicities between 5 d^{-1} and 144 d^{-1}, we chose to exclude all frequencies below 5 d^{-1} in our search. Thus the excluded frequency ranges were < 5 d^{-1}, 14 ± 0.1 d^{-1}, 15 ± 0.1 d^{-1}, 29 ±

0.1 d^{-1}, 30 ± 0.1 d^{-1}, 44 ± 0.1 d^{-1}, 45 ± 0.1 d^{-1}, and so on.

Although the sources examined are the 230 brightest sources observed by the ASM, they span a large range in intensity. Figure 4-1 shows the power density spectrum of strong source KS 1731-260. Note that the 15 d^{-1} peak and its harmonics are clearly present in the whitened spectrum. In addition, the 15 d^{-1} peak displays two weaker peaks at 14 d^{-1} and 13 d^{-1}. These peaks clearly represent beats with the 1 d^{-1} orbital frequency of the Earth. In contrast, weaker sources do not display these artifacts so clearly. Thus the search process outlined in the previous paragraph must be modified based on the overall intensity of the source.

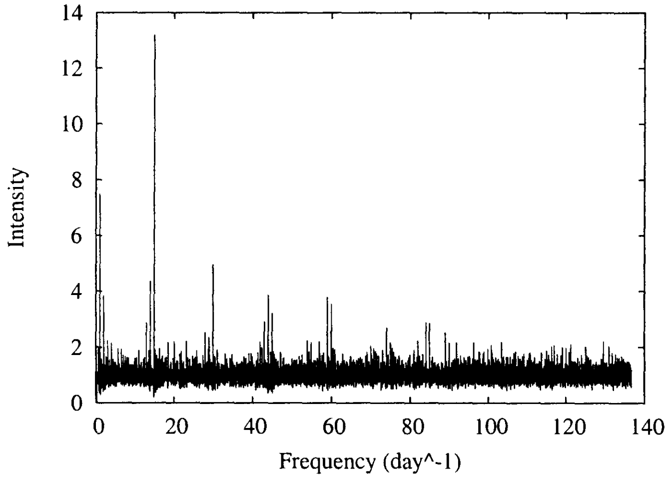

Figure 4-1: Power density spectrum of KS 1731-260 after maximum-rebinning and local averaging

Power spectra from strong sources, such as the one shown in Figure 4-1, tend to have an overall higher power amplitude. The artifacts are stronger, and the mean baseline is higher than in weaker sources. Thus we decided to search the strong sources using a higher intensity threshold. To determine a new threshold, we lowered the expected number of statistically significant peaks to 0.1 and repeated the calculation shown in Section 4.1. This process gives $I_0 = 3.89$, which we take as the threshold for intense sources. The excluded frequency range also had to be modified because the strong sources tend to show more than one observable beat. For example, the spectrum in Figure 4-1 has a beat at 14 d^{-1} *and* 13 d^{-1}. Therefore we add 13 ± 0.1

d^{-1} and 28 ± 0.1 d^{-1} to the range of excluded frequencies.

4.3 Search Results

The periodicities of four X-ray sources with known orbital periods – AM Her, Cyg X-3, EXO 0748-676, and X1916-053 – were observed and verified in this search. In addition, we identified statistically significant periodicities in four sources. The X-ray modulation in one of these sources, GX 9+9, had been observed before, although never with the ASM. The periodicity found in XTE J1723-376 is a new result and could be an orbital frequency.

Known Periodicities

Four previously known orbital frequencies were detected in the search method outlined above. **AM Her** is an X-ray source with a known periodicity of 7.75644 d^{-1}. As seen in Figure 3-2, the search verified this frequency.

Cyg X-3 is the compact object of a HMXB system [11]. The companion is a Wolf-Rayet star losing mass at a high rate through a stellar wind. The source is known to have an orbital frequency of 5.0073 ± 0.0003 d^{-1} [12]. Figure 4-2 shows the power density spectrum of Cyg X-3 after analysis. The spectrum is dominated by the peak at 5.00777 d^{-1}, which agrees with the known value.

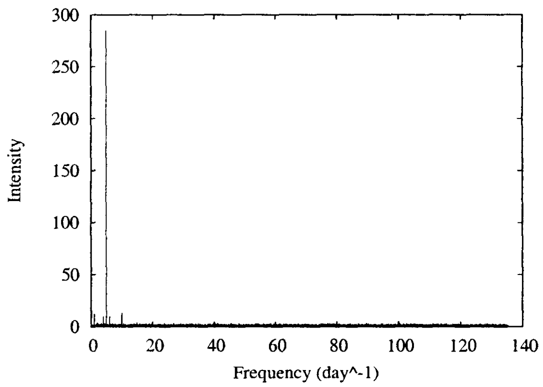

Figure 4-2: Power Density spectrum of Cyg X-3. The strongest peak in the spectrum is at the orbital frequency of 5.00777 d^{-1}.

EXO 0748-676 is the neutron star in a LMXB system that shows quasi-periodic oscillations [13]. The system shows very strong intensity dips and eclipses of the companion star [14]. The orbital frequency of the system is established at 6.27597 ± 0.00001 d^{-1} [15]. In Figure 4-3, this peak appears with a power of 3.9 at 6.27593 ± 0.00005 d^{-1}, which agrees with the known value.

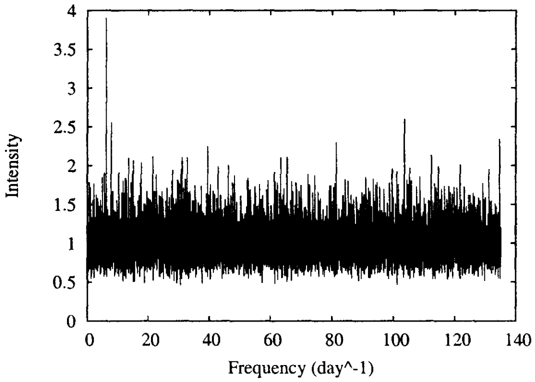

Figure 4-3: Power Density spectrum of EXO 0748-676. The strongest peak in the spectrum is at the orbital frequency of 6.27593 d^{-1}.

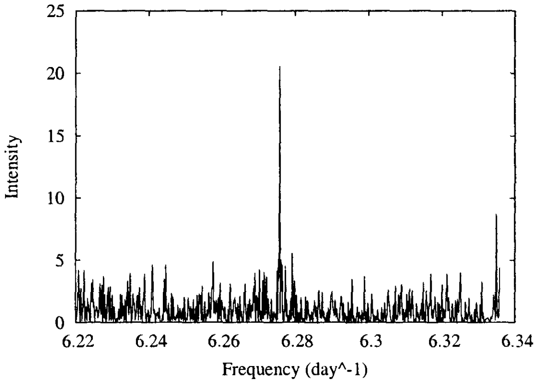

Figure 4-4: Power Density spectrum of EXO 0748-676 before rebinning or local averaging. The FWHM of the peak is three frequency bins and the amplitude of the peak is 20.613, corresponding to 0.00005 d^{-1}.

X 1916-053 is the compact object of an LMXB dipping source [16]. The orbital frequency of the system has been measured in the X-ray energy band at 28.793754 ± 0.000009 d^{-1} and in the optical band at 28.53792 ± 0.00005 d^{-1}[16]. Figure 4-5 shows the power density spectrum, where the first harmonic is detected at 57.58745

d^{-1}. From Figure 4-6, the uncertainty of the peak is 0.00009 d^{-1}. This value for the first harmonic is within 0.5 standard deviation of the frequency previously reported in the X-ray band. However, the frequency found in this search does not agree with the optical periodicity by over 5000 standard deviations.

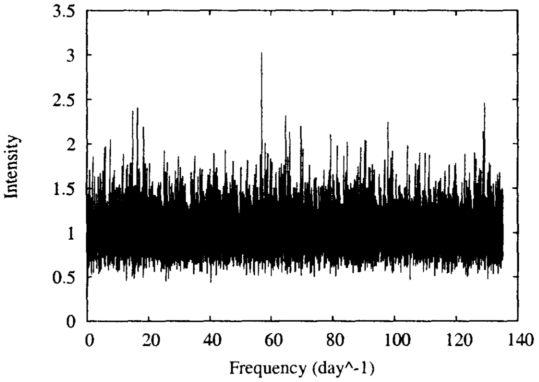

Figure 4-5: Power Density spectrum of X1916-053. Although the peak at 57.58745 d^{-1} is the strongest one in the spectrum, it is less significant than the periodicities in Figures 4-2 and 4-3.

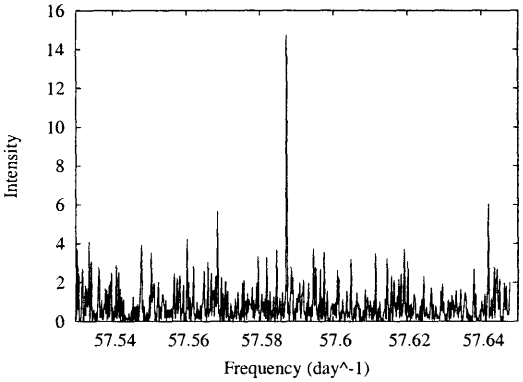

Figure 4-6: Power Density spectrum of X1916-053 before rebinning or local averaging. The FWHM of the peak is four frequency bins, corresponding to 0.00009 d^{-1}.

Periodicities Found in this Search

Figure 4-7 shows the ASM light curves of the four sources for which this search found a new periodicity.

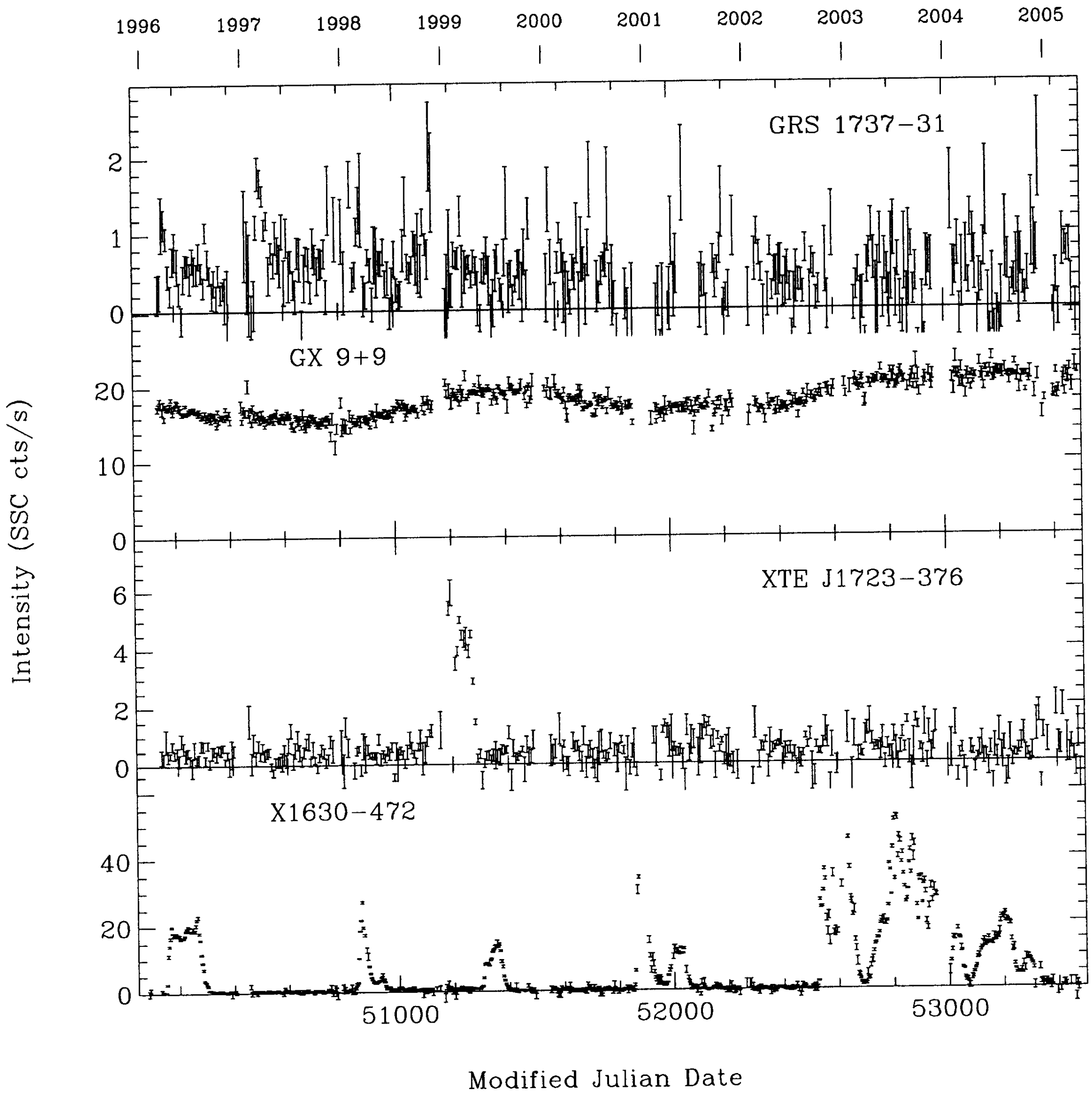

Figure 4-7: ASM Light Curves for sources with new periodicities in the 1.5-12 keV energy band. With the exception of GX 9+9, which is consistently bright,the sources are transient and exhibit outburst behavior. Figure courtesy A. Levine.

X1630-472 is a transient LMXB that displays outbursts every 550-690 days [17]. Spectral analysis suggests that this source is a black hole candidate. In Figure 4-8, a peak in the power density spectrum is apparent at 113.605 d^{-1} with a power amplitude of 4.17. R. Remillard used the more more powerful *RXTE* Proportional Counter Array (PCA) to search for this peak in the power density spectrum of X1630-472. The search did not find a peak at 113.6046 d^{-1}, suggesting that it may not be a periodicity of the source. Also apparent in this spectrum are the strong peak at 1 d^{-1} and the peaks at 15 d^{-1} and 30 d^{-1}.

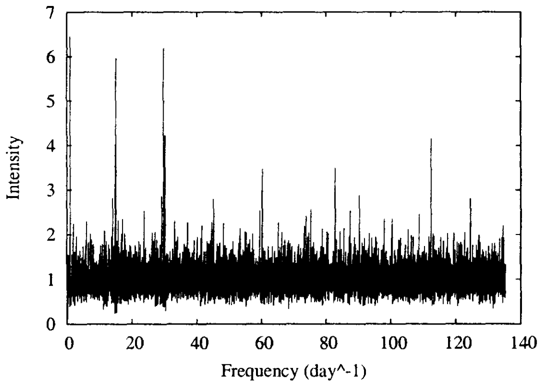

Figure 4-8: Power Density spectrum of X1630-472. A strong peak appears at 113.6046 d^{-1}.

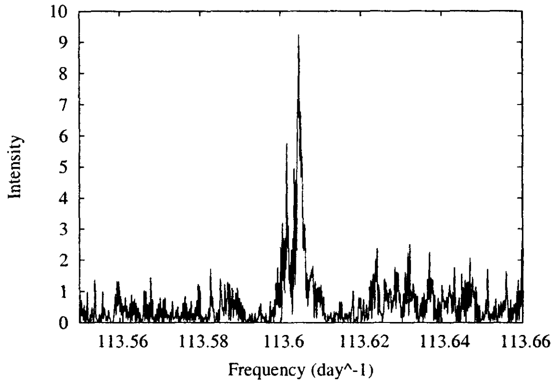

Figure 4-9: Power Density spectrum of X1630-472 before rebinning or local averaging. The FWHM of the peak is fifteen frequency bins and the amplitude is 9.249, corresponding to an uncertainty of 0.0004 d^{-1}.

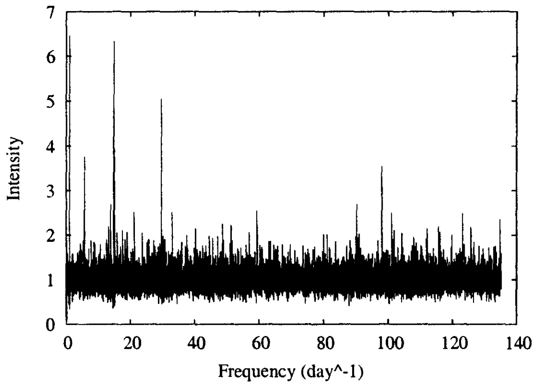

Figure 4-10: Power Density spectrum of GX 9+9. The orbital frequency appears as a peak at 5.72323 d^{-1}.

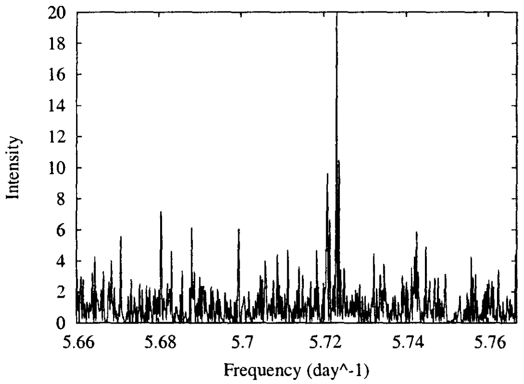

Figure 4-11: Power Density spectrum of GX 9+9 before rebinning or local averaging. The FWHM of the peak is four frequency bins and the amplitude is 19.914, corresponding to an uncertainty of 0.00007 d^{-1}.

GX 9+9 is an LMXB whose periodic modulations have been observed in both X-ray and optical wavelengths [13, 14]. The companion star is a main-sequence star that fills its Roche lobe. Optical observations show that it appears as a faint blue star with an intensity modulation of 4.198 ± 0.0094 hr [19]. Observations in the 0.5-20 keV energy band, which lies in the X-ray range, also show an intensity modulation of 4.19 ± 0.02 hr [18]. Figure 4-10 shows the power density spectrum of GX 9+9. The peak at 5.72323 d^{-1} is weaker than the artifacts at 15 d^{-1} and 30 d^{-1}. We are confident in the peak's statistical significance, however, because it does not lie close to any region identified as an artifact. Although the X-ray modulation of this source has been well established, this marks the first time it has been observed in ASM data.

The frequency found for this peak corresponds to a period of 4.19344 ± 0.00005 hr, which agrees with the orbital frequency reported earlier in both the X-ray and the optical wavelengths.

GRS 1737-31 is a transient X-ray source located near the Galactic center [20]. Spectral analysis suggests that this source is also a black hole candidate with light curve behaviour resembling that of Cygnus X-1, a well-known black hole candidate. A peak at 124.66588 d^{-1} appears in the power density spectrum, shown in Figure 4-12. This corresponds to a period of 693.05 s, which could be the rotation period of a pulsar.

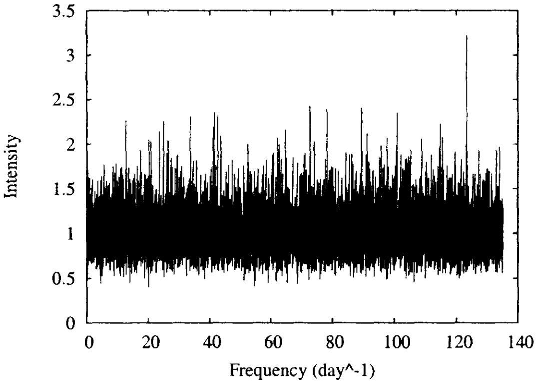

Figure 4-12: Power Density spectrum of GRS 1737-31. Although the peak at 124.66588 d^{-1} has an amplitude of 3.22, it may be significant because the source is a weak one.

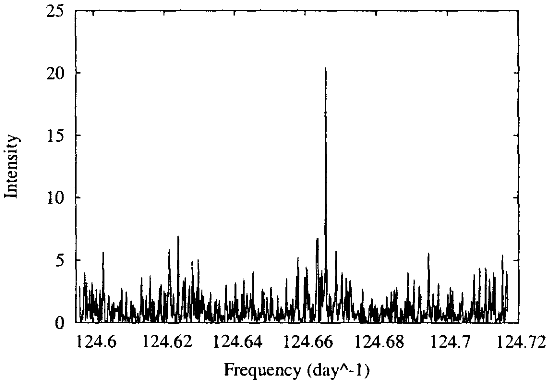

Figure 4-13: Power Density spectrum of GRS 1737-31 before rebinning or local averaging. The FWHM of the peak is four frequency bins and an amplitude of 20.459, corresponding to 0.00007 d^{-1}.

XTE J1723-376 is a transient source that experienced an outburst for about 160 days during 1999 (see Figure 4-7). There has not been a previously reported periodicity for this source. Figure 4-14 shows the power density spectrum, which has a peak at 6.0999 d^{-1} and power amplitude of 3.95. As in the case for GX 9+9, this peak is not as strong as the peaks at 15 d^{-1} and 30 d^{-1}. But because it is confined to a single rebinned frequency bin, and it is not near a known artifact, it is reasonable to guess that it is a real peak. Figure 4-15 shows the power density spectrum calculated during the outburst time interval of 51140-51300 MJD. The peak at 6.09994 d^{-1} is not statistically significant during the outburst. Figure 4-16 shows the spectrum calculated by excluding the outburst, and the peak is again visible. This suggests that the peak at 6.09994 d^{-1} is not a periodicity inherent to the source, but we cannot rule out the possibility.

Table 4.1 summarizes the results from the periodicity search. Listed periodicities were found in the sum energy band of 1.5-12 keV. The last column states other energy bands that showed the periodicity. Note that the periodicity found for X1916-053 is the first harmonic of the frequency reported in [16].

Table 4.1: Periodicities dectected in ASM data in the 1.5-12 keV range

Source	Frequency	Amplitude	Additional Energy Bands
Known Periodicities			
Cyg X-3	5.00777 ± 0.00003 d^{-1}	284.85	1.5-3keV, 3-5 keV, 5-12 keV
EXO 0748-676	6.27593 ± 0.00005 d^{-1}	3.90	3-5 keV
AM Her	7.75644 ± 0.00009 d^{-1}	5.86	5-12 keV
X1916-053	57.58745 ± 0.00009 d^{-1}	3.03	1.5-3 keV
Suspected Periodicities			
GX 9+9	5.72323 ± 0.00007 d^{-1}	4.02	5-12 keV
XTE J1723-376	6.09994 ± 0.00007 d^{-1}	3.46	3-5 keV
X1630-472	113.6046 ± 0.0004 d^{-1}	4.17	3-5 keV, 5-12 keV
GRS 1737-31	124.66588 ± 0.00007 d^{-1}	3.22	

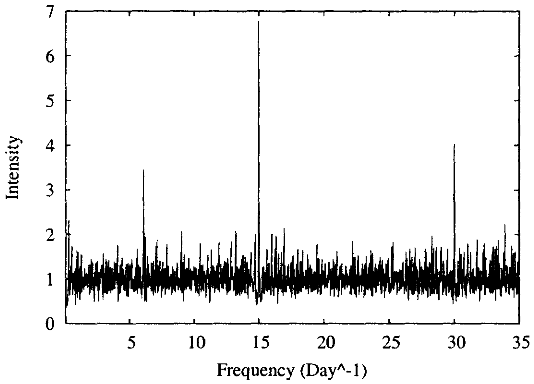

Figure 4-14: Power Density spectrum of XTE J1723-376. The suspected periodicity appears as a peak at 6.09994 d^{-1}.

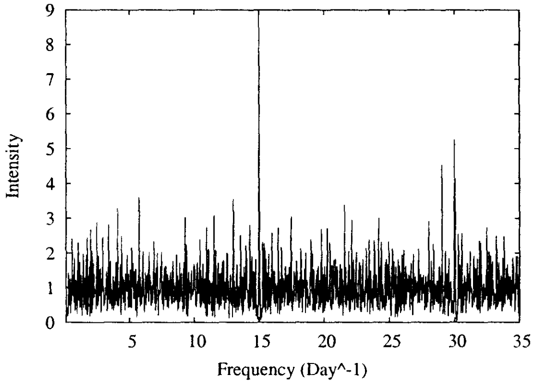

Figure 4-15: Power Density spectrum of XTE J1723-376 during the outburst time interval of 51140-51300 MJD.

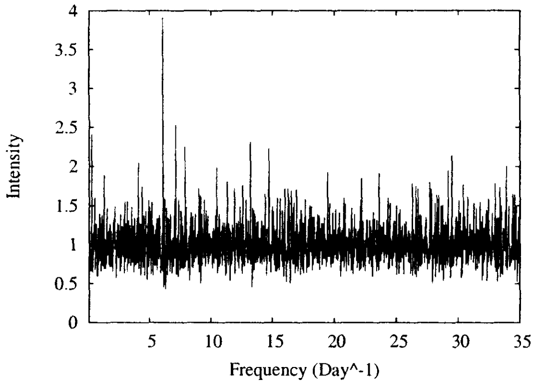

Figure 4-16: Power Density spectrum of XTE J1723-376 excluding the outburst time interval. The orbital frequency is again visible at 6.09994 d^{-1} with a power amplitude of 3.95.

References

[1] M. Zeilik and S.Gregory, *Introductory Astronomy and Astrophysics* (1998).

[2] http://imagine.gsfc.nasa.gov/docs/science/know_12/dwarfs.html

[3] N.E. White, F. Nagase, and A.N. Parmar, "The Properties of X-Ray Binaries" in *X-Ray Binaries* (1995).

[4] D. Psaltis, astro-ph/0410536 (2004).

[5] from http://science.nasa.gov/newhome/headlines/ast19sep97_3.htm

[6] L. Bildsten, ApJ. 501 (1998) L89.

[7] from http://astrosun2.astro.cornell.edu/academics/courses/astro201/roche_lobe.htm

[8] A. Levine et al, ApJ. (Proc. Suppl) 69/1-3 (1998) 196.

[9] *XTE Timing Explorer: Taking the Pulse of the Universe* (1992).

[10] D. Crampton and A.P. Cowley, Astro. Soc. Pacific 89 (1977) 374-385.

[11] http://am.ub.es/~josep/cygX3/English/cygx3/eng_cyg.html.

[12] N.S. Singh et al, Bull. Astr. Soc. India 29 (2001) 351-354.

[13] A.N. Parmar, A.P. Smale, F. Verbunt, and R.H. Corbet, ApJ. 366 (1991) 253-260.

[14] J. Homan and M. Van der Klis, ApJ 539 (2000) 847-850.

[15] A.N. Parmar, N.E. White, P. Giommi, and M. Gottwald, ApJ. 308 (1986) 199-212.

[16] Y. Chou, J.E. Grindlay, and P.F. Bloser, ApJ. 549 (2001) 1135-1144.

[17] D. Tournear et al, AAS (2002) 201.1506T.

[18] P. Hertz and K. Wood, ApJ 331 (1988) 764-772.

[19] B. Schaefer, Astophys. J, 354 (1990) 720-725.

[20] W. Cui et al, ApJ 487L (1997) 73c.